

Decay of $^{150,158}\text{Tb}^*$ nuclear systems formed in reactions induced by loosely bound ^6Li

Gurvinder Kaur and Manoj K. Sharma*

School of Physics and Materials Science, Thapar University, Patiala - 147004, Punjab, India

(Received 8 January 2013; published 3 April 2013)

In reference to recent experiments, the collective clusterization approach is employed to investigate the dynamics of $^6\text{Li} + ^{144,152}\text{Sm}$ reactions over a wide range of incident energies spread across the Coulomb barrier. In order to account for the role of deformations, the cross sections for the $^6\text{Li} + ^{152}\text{Sm} \rightarrow ^{158}\text{Tb}^* \rightarrow A_1 + A_2$ reaction have been studied using a spherical choice of fragmentation, and by considering static $\beta_{2i}(0)$ and dynamic $\beta_{2i}(T)$ quadrupole deformations within the optimum orientations θ_i^{opt} approach. Furthermore, the orientation degree of freedom is shown to play an important role, and the same has been investigated by considering equatorial (compact) as well as polar (noncompact) orientational features. The role of level density parameter, barrier modification, and angular momentum dependence is duly addressed. Also, the shell closure effect and the N/Z dependence of decay fragments have been explored in context of the fragmentation process of $^{150,158}\text{Tb}$ nuclei. Finally, the incomplete fusion process (ICF) observed due to break up of loosely bound projectile ^6Li on the deformed target ^{152}Sm is worked out.

DOI: [10.1103/PhysRevC.87.044601](https://doi.org/10.1103/PhysRevC.87.044601)

PACS number(s): 25.70.Gh, 25.70.Jj, 25.60.Gc

I. INTRODUCTION

The study of reactions induced by stable loosely bound nuclei are of immense importance so far as the heavy ion reaction dynamics is concerned. This is because, in such reactions, the fusion process has a more intricate character because of the high probability of breakup caused by the low binding energy of the loosely bound nuclei (e.g., ^6Li , ^9Be , etc.) involved. This may be attributed to the anomalous structure of loosely bound nuclei, owing to which their behavior towards the fusion process is different from that of tightly bound nuclei. Thus, understanding the dynamics of loosely bound nuclei is of considerable importance. However, for the overall understanding of structure effects and the dynamics involved in such reactions, one also needs to investigate the effect of deformations and orientations of the colliding nuclei as well as the decaying fragments.

In a recent experiment [1], with the use of a ^6Li beam on a ^{152}Sm target, the fusion excitation functions have been measured for a $^{158}\text{Tb}^*$ nucleus at various incident energies varying from $E_{\text{lab}} = 20\text{--}40$ MeV (equivalently $E_{\text{c.m.}} = 19.2\text{--}38.5$ MeV) lying across the Coulomb barrier. The complex process of fusion involving deformed light mass projectile and heavy target nuclei can be best understood via the decay study of compound nucleus formed. In view of this, the decay cross sections for $^{158}\text{Tb}^*$ formed in the $^6\text{Li} + ^{152}\text{Sm}$ reaction have been tested in the framework of the dynamical cluster-decay model (DCM) of Gupta and collaborators [2–10]. In general, fusion cross sections are considered to have a contribution from evaporation residue, σ_{ER} consisting of multiple light particles ($A_2 \leq 4$) such as neutron, proton, α particle, γ ray, etc., and from the fission cross section, σ_{fission} i.e., $\sigma_{\text{fusion}} = \sigma_{\text{ER}} + \sigma_{\text{fission}}$ along with a contribution of some noncompound nucleus (nCN) processes, if any. However, for the lanthanide system under consideration, the fusion cross sections are

observed to have a contribution from ER alone, while the fission contribution is negligible. Thus for the $^6\text{Li} + ^{152}\text{Sm} \rightarrow ^{158}\text{Tb}^*$ reaction, $\sigma_{\text{fusion}} \sim \sigma_{\text{ER}}$. Since, the projectile, target involved and the compound nucleus formed are all deformed so the role of deformations and orientations is expected to be of importance for the present system. Interestingly, DCM, having both these degrees of freedom included into it, has the ability to provide furtherance for the study of such reactions. Another interesting aspect of the reaction under consideration is the possible role of shell effects [11] of the decaying fragments. The presence of such effects suggest the involvement of some competing nCN process in addition to the compound nucleus decay [12]. The role of deformations and the shell closure effects are explored by making a comparative study of the decay of $^{158}\text{Tb}^*$ nucleus with $^{150}\text{Tb}^*$ formed in the reaction induced by ^6Li on spherical target ^{144}Sm [13].

The measured cross sections in [1] show $\sim 28\%$ suppression of fusion cross sections for the $^{158}\text{Tb}^*$ nucleus at above barrier energies. This suppression is associated with the break-up process in which the projectile (loosely bound nucleus) breaks up prior to reaching the fusion barrier and gives rise to the incomplete-fusion process. The interest in understanding the influence of the break up of loosely bound nuclei on fusion has indeed received a fillip [14] because of the change in nature of the reaction products, investigated for loosely bound nuclei [15]. It is well known that at the higher energies when processes other than the complete fusion become important, the fusion cross sections are found to drop below the total reaction cross sections. In other words it can be said that it is due to this break-up tendency, that the complete fusion cross sections in such reactions are suppressed. Consequently, the missing complete fusion cross section can be found in the yield of incomplete fusion (ICF). A systematic study of the decay of such reactions can reveal useful information about the dynamics involved in the process.

The urge behind the study of this lanthanide system is (i) the indispensable role of deformation of the colliding as well as the decaying fragments. To pursue with it, the

* msharma@thapar.edu

deformations effect on decaying fragments are studied by taking into account spherical and quadrupole (β_2) deformed choice of fragmentation. Apart from deformations, the role of hot (equatorial) and noncompact (polar) orientations is also studied in this work. (ii) A comparative study of isotopes of the lanthanide system, i.e., $^{150,158}\text{Tb}^*$ formed in $^6\text{Li} + ^{144,152}\text{Sm}$ reactions. (iii) The role of shell effects of decaying fragments in $^{150}\text{Tb}^*$ and $^{158}\text{Tb}^*$ nuclear systems. (iv) The role of loosely bound nucleus ^6Li as projectile, which undergoes break-up and brings into account the incomplete fusion process (ICF).

The organization of this paper is as follows. A brief account of the dynamical cluster-decay model (DCM) is presented in Sec. II. The calculations and results for excitation functions of both CF and ICF processes are discussed in Sec. III. Finally, results are summarized in Sec. IV.

II. THE DYNAMICAL CLUSTER-DECAY MODEL (DCM)

In DCM [2–10], the decay of compound nucleus (CN) into both the Evaporation residues (ERs) and fission fragments is treated as dynamical collective mass motion of preformed clusters or fragments through the interaction barrier. This approach provides an alternative method to address the decay mechanism of compound nuclear systems formed in heavy ion reactions.

Based on the well known quantum mechanical fragmentation theory (QMFT) [16–18], DCM is worked out in terms of the collective coordinates of mass (and charge) asymmetries $\eta_A = (A_1 - A_2)/(A_1 + A_2)$ [and $\eta_Z = (Z_1 - Z_2)/(Z_1 + Z_2)$, 1 and 2 stand, respectively, for heavy and light fragments], the relative separation R to which is also added the multipole deformations $\beta_{\lambda i}$ ($\lambda = 2, 3, 4$), and orientations θ_i ($i = 1, 2$) of two nuclei or fragments. In terms of these coordinates the compound nucleus decay or fragment production cross section for ℓ -partial waves is given by

$$\sigma = \sum_{\ell=0}^{\ell_{\max}} \sigma_{\ell} = \frac{\pi}{k^2} \sum_{\ell=0}^{\ell_{\max}} (2\ell + 1) P_0 P; \quad k = \sqrt{\frac{2\mu E_{c.m.}}{\hbar^2}}, \quad (1)$$

where $\mu = [A_1 A_2 / (A_1 + A_2)]m$ is the reduced mass, and ℓ_{\max} is the maximum angular momentum, decided at a point where evaporation residue cross section becomes negligibly small, $\sigma_{\text{ER}} \rightarrow 0$.

In Eq. (1) the preformation probability P_0 , given as

$$P_0 = |\psi(\eta(A_i))|^2 \sqrt{B_{\eta\eta}} \frac{2}{A_{\text{CN}}}, \quad (2)$$

refers to η motion and is obtained by solving the stationary Schrödinger equation in η , at a fixed $R = R_a$. The preformation probability P_0 is an important factor in DCM as it provides relevant structural aspects and imparts information of a decaying nucleus which is missing in statistical models. Since, in the competing noncompound ICF channel, a part of the projectile interacts with a target so P_0 is calculated in similar way as that for the CN process, with the only difference that ICF leads to a different composite system depending on the break up of the projectile nucleus.

The fragmentation potential $V_R(\eta, T)$ is defined as

$$V_R(\eta, T) = \sum_{i=1}^2 [V_{\text{LDM}}(A_i, Z_i, T)] + \sum_{i=1}^2 [\delta U_i] \exp(-T^2/T_0^2) + V_C(R, Z_i, \beta_{\lambda i}, \theta_i, T) + V_P(R, A_i, \beta_{\lambda i}, \theta_i, T) + V_{\ell}(R, A_i, \beta_{\lambda i}, \theta_i, T). \quad (3)$$

Here V_C , V_P , and V_{ℓ} are, respectively, the T -dependent, Coulomb, nuclear proximity, and angular momentum dependent potentials for deformed, oriented nuclei with the moment of inertia taken in the complete sticking limit. The $V_R(\eta, T)$ at each temperature (T) is calculated as Strutinsky macro-microscopic method, where the macroscopic term V_{LDM} is the T -dependent liquid drop energy of Davidson *et al.* [19], with its constants at $T = 0$ refitted [20] to give the recent experimental binding energies [21], and the microscopic shell corrections δU are the “empirical” estimates of Myers and Swiatecki [22], also taken as T -dependent.

The penetration probability P in Eq. (1) refers to R -motion and is calculated using the WKB integral as

$$P = \exp\left[-\frac{2}{\hbar} \int_{R_a}^{R_b} \{2\mu[V(R) - Q_{\text{eff}}]\}^{1/2} dR\right], \quad (4)$$

where R_a , the first turning point of the barrier penetration, is defined as

$$R_a = R_1(\alpha_1, T) + R_2(\alpha_2, T) + \Delta R(T) = R_t(\alpha, T) + \Delta R(T) \quad (5)$$

with radius vectors ($i = 1, 2$)

$$R_i(\alpha_i, T) = R_{0i}(T) \left[1 + \sum_{\lambda} \beta_{\lambda i} Y_{\lambda}^{(0)}(\alpha_i)\right] \quad (6)$$

and T -dependent nuclear radii $R_{0i}(T)$ of the equivalent spherical nuclei [23],

$$R_{0i}(T) = [1.28 A_i^{1/3} - 0.76 + 0.8 A_i^{-1/3}] (1 + 0.0007 T^2). \quad (7)$$

In the definition of R_a above, ΔR is the relative separation distance between two fragments or clusters A_i . It decides the first turning point of barrier penetration, referring to actually used barrier height and also allows us to define, equivalently, the barrier lowering parameter ΔV_B , which relates $V(R_a, \ell)$ and the top of the barrier $V_B(\ell)$, for each ℓ , as

$$\Delta V_B(\ell) = V(R_a, \ell) - V_B(\ell). \quad (8)$$

One may see that the actually used barrier is effectively lowered as the entry level of the penetration point is always lower than the barrier height.

For deformations $\beta_{\lambda i}$, the static deformations in DCM are taken from the theoretical estimates of Möller and Nix [24], and the temperature dependence in the deformations are considered via [25,26], and are given as

$$\beta_{\lambda i}(T) = \exp(-T/T_0) \beta_{\lambda i}(0), \quad (9)$$

where $\beta_{\lambda i}(0)$ are the static deformations and T_0 is the temperature of the nucleus at which shell effects start to vanish.

Also, the optimum orientations θ_i^{opt} of the hot fusion process for β_{2i} choice of fragmentation are taken from Ref. [10].

The temperature (T) is related to CN excitation energy as

$$E_{\text{CN}}^* = aT^2 - T. \quad (10)$$

In the framework of DCM, 'a' is generally taken as $A_{\text{CN}}/9$.

III. CALCULATIONS AND DISCUSSION

The formation cross sections of compound nucleus $^{158}\text{Tb}^*$ formed in the $^6\text{Li} + ^{152}\text{Sm}$ reaction have been investigated recently [1] at different incident energies varying from $E_{\text{c.m.}} = 19.2\text{--}38.5$ MeV, lying across the Coulomb barrier and the same has been tested here using the dynamical cluster-decay model (DCM). The evaporation residue decay mode forms an unambiguous tool for the study of nuclear reactions and the same is explored in this work, since, for the lanthanide system studied here, the measured complete fusion cross sections are mainly associated with ER contribution. For the $^6\text{Li} + ^{152}\text{Sm}$ reaction the role of deformations (across the barrier) and orientations (particularly at below barrier region) is studied for which the calculations have been done using a spherical choice of fragmentation, with the inclusion of static deformation $\beta_{2i}(0)$ and with the dynamic deformed $\beta_{2i}(T)$ choice of fragmentation in reference to optimum (θ_i^{opt}) orientation approach. Also, experimentally a suppression of $\sim 28\%$ in the complete fusion cross section has been observed. This suppression is accounted in the form of an incomplete fusion (ICF) process and is treated in the framework of DCM. We have divided this section into three subsections. The role of static and dynamic quadrupole deformations is discussed in Sec. III A. The application of DCM in reference to $^{150}\text{Tb}^*$ formed by spherical target ^{144}Sm instead of deformed target ^{152}Sm is discussed in Sec. III B. In addition to the effect of target deformation, this comparison helps us to investigate the isotopic effect that is produced due to the addition of $8n$ in going from the $^{150}\text{Tb}^*$ to the $^{158}\text{Tb}^*$ nucleus. Also, the shell closure effect of decaying fragments is duely addressed in this section. Finally, the cross sections for the incomplete fusion (ICF) process observed due to loosely bound projectile ^6Li are discussed in Sec. III C.

A. Role of deformations in decay of $^{158}\text{Tb}^*$

Following the experimental data [1] we tried to fit the ER cross sections by considering the spherical and quadrupole deformed choice of fragmentation within the optimum orientation approach. The role of deformations in decaying fragments is studied by considering three different choices of fragmentation paths: (i) spherical path, (ii) static deformed fragmentation path, in which the deformations are independent of temperature, and (iii) dynamic deformations having the effect of temperature included in it. The scattering potential in Fig. 1, plotted at $E_{\text{c.m.}} = 19.2$ MeV (and $T = 1.26$ MeV) for extreme angular momentum values, $\ell = 0\hbar$ and $\ell = \ell_{\text{max}}$, shows the effect of deformation on the barrier position and barrier height. In the figure, solid lines represent spherical fragmentation, dotted lines are for static $\beta_{2i}(0)$ deformations,

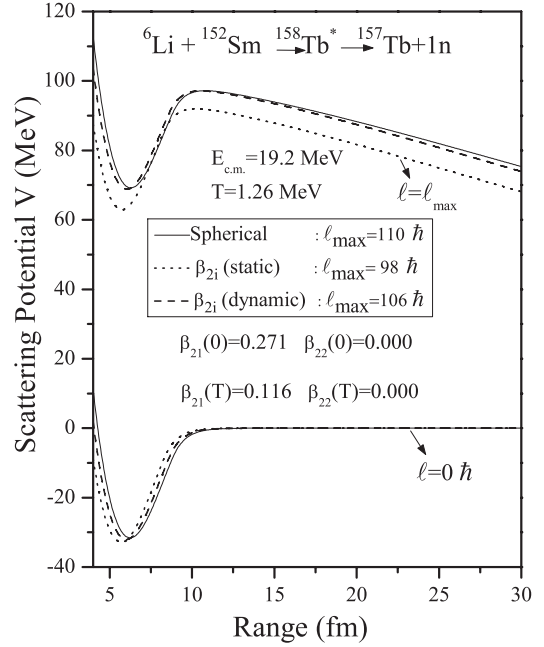


FIG. 1. The scattering potential $V(R)$ for the decay of $^{158}\text{Tb}^* \rightarrow ^{157}\text{Tb} + n$ at extreme ℓ values for spherical, static $\beta_{2i}(0)$ deformed, and dynamic $\beta_{2i}(T)$ deformed choice of fragmentation.

and the dashed lines denote dynamical $\beta_{2i}(T)$ deformations. It is observed that with the inclusion of static $\beta_{2i}(0)$ and dynamic $\beta_{2i}(T)$ quadrupole deformations both the barrier position as well as height get modified and hence the fusion probability gets influenced.

Figure 2 shows the fragmentation potential $V(A_2)$ minimized in mass co-ordinate η_A , for the $^6\text{Li} + ^{152}\text{Sm} \rightarrow ^{158}\text{Tb}^*$ reaction at two extreme energies across the barrier, i.e., at $E_{\text{c.m.}} = 19.2$ MeV ($T = 1.26$ MeV) and $E_{\text{c.m.}} = 38.5$ MeV ($T = 1.65$ MeV). In order to study the role of deformations, we have plotted the fragmentation potential for spherical, static $\beta_{2i}(0)$ deformed, and dynamic $\beta_{2i}(T)$ deformed choices of fragmentation. The interesting points observed from this figure are (i) the characteristic behavior of the fragmentation potential is different at lower versus higher ℓ values. The behavior at the maximum angular momentum value, i.e., $\ell = \ell_{\text{max}}$ is illustrated in Figs. 2(a) and 2(b) whereas Figs. 2(c) and 2(d) show the behavior at $\ell = 0\hbar$. It is observed that deformations play a significant role at $\ell = \ell_{\text{max}}$ but are silent at $\ell = 0\hbar$. (ii) At $\ell = \ell_{\text{max}}$, the structure of the fragmentation potential is almost similar for spherical and dynamic deformations but is different for static deformations. At relative grounds the fragmentation potential is minimum for the static deformations and the α structure is more prevalent for the deformed choice of fragmentation. (iii) Except for the change in the magnitude of the fragmentation potential, no noticeable change in the structure of $V(A_2)$ is observed while going from lower to higher energy, for spherical and dynamical deformed fragmentations at $\ell = 0\hbar$ and $\ell = \ell_{\text{max}}$. Whereas with the inclusion of static deformation, a small change in the structure of fragments having mass $A_2 = 14\text{--}30$ is observed at higher angular momentum. Thus, one may conclude that the fragmentation path is almost independent of the variation in energy. Using the

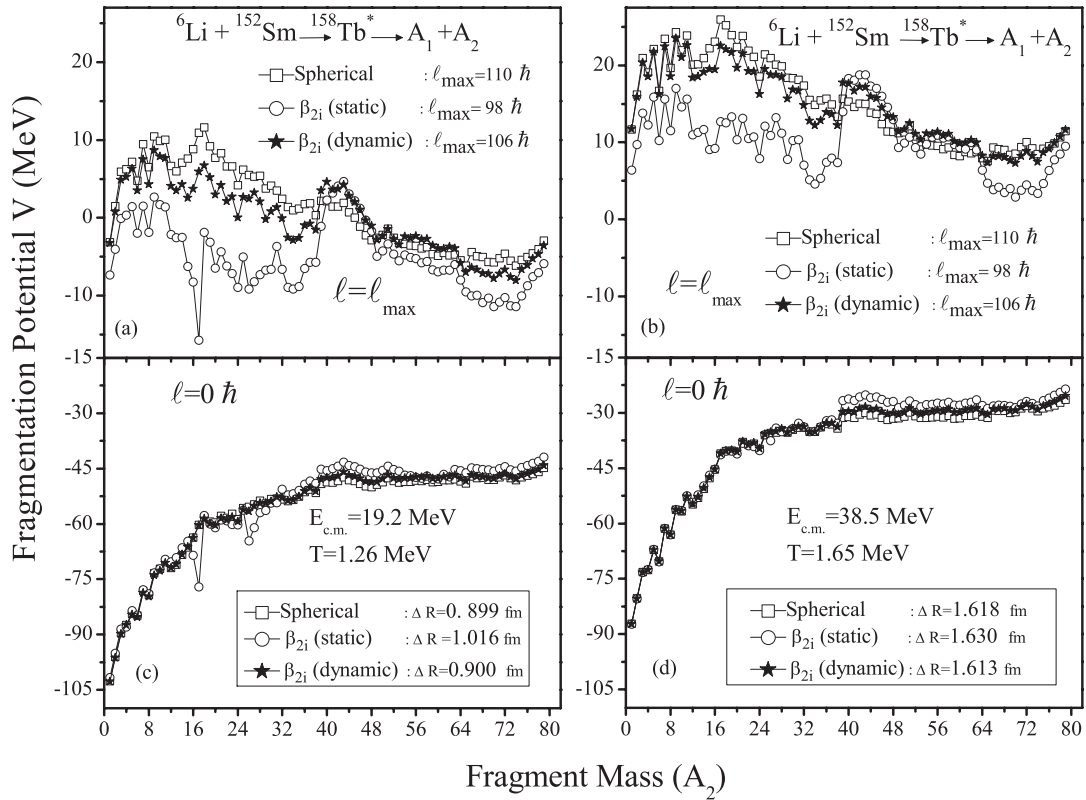


FIG. 2. Fragmentation potential as a function of light fragment mass no. (A_2), for the decay of $^{158}\text{Tb}^*$ formed in $^6\text{Li} + ^{152}\text{Sm}$ reaction at (a), (c) $E_{\text{c.m.}} = 19.2$ MeV and (b), (d) $E_{\text{c.m.}} = 38.5$ MeV using spherical and deformed choices of fragmentation ($\beta_2, \theta_i^{\text{opt}}$).

DCM approach, the cross section for ER ($A_2 \leq 4$) has been fitted within one parameter fitting, i.e., neck-length parameter ΔR . This means that for different values of ΔR , we have attained the reported ER cross sections for all three choices of fragmentation. The values of ΔR for spherical and dynamic $\beta_{2i}(T)$ deformed cases are comparable to each other, being 0.899 fm and 0.9 fm at $E_{\text{c.m.}} = 19.2$ MeV and 1.618 fm and 1.613 fm at $E_{\text{c.m.}} = 38.5$ MeV, respectively. Whereas, it is relatively higher in magnitude for the static $\beta_{2i}(0)$ deformation approach being 1.016 fm at $E_{\text{c.m.}} = 19.2$ MeV and 1.630 at $E_{\text{c.m.}} = 38.5$ MeV.

The effect of the deformed configuration is also evident from Fig. 3 which shows a variation of the preformation probability P_0 as a function of fragment mass A_i . The figure clearly supports the fact that the role of deformations comes into picture at higher angular momentum while it remains silent at $\ell = 0\hbar$. On a broader view, it is observed that the fission fragment mass distribution is symmetric for all three choices of fragmentation for both energies at $\ell = \ell_{\text{max}}$. However, a specific look at Figs. 3(a) and 3(b) shows that the mass distribution of spherical and $\beta_{2i}(T)$ is similar but that of $\beta_{2i}(0)$ is quite different. Also, the emergence of IMFs and HMFs (lying within mass range $A_2 = 14-30$) is observed for either of the chosen energies across the barrier for the $\beta_{2i}(0)$ choice of fragmentation. This emergence of IMFs and HMFs along with observed symmetric fragmentation indicates a possibility of fine structure effects in the decay of the $^{158}\text{Tb}^*$ nucleus. In conclusion, the inclusion of deformation

and orientation effects of the decaying fragments change the relative preformation probability P_0 quite significantly, and hence, equivalently, the potential energy surface (PES).

Interestingly, in the experiment [1], at higher energies the contribution of the charged particle is also indicated but not identified. The DCM based calculations identify the charged particle involved in the decay of the $^{158}\text{Tb}^*$ nucleus. The calculations suggest that a ^4H charged particle contributes about $\sim 1\%$ towards the ER cross section of the $^{158}\text{Tb}^*$ nucleus. It is relevant to mention here that in the context of DCM calculations the $1n$ channel contributes the most towards the ER cross section followed by σ_{xn} ($x = 2, 3, 4, 5$) and ^4H decay. However, if one takes relatively higher values of neck-length parameter ΔR then the reported cross section could be achieved without including the $1n$ cross section. These results are discussed later in Fig. 6.

It may be noted further that the barrier modification is an in-built property of DCM, that enters through neck-length parameter ΔR . Figure 4(a) shows a variation of the barrier lowering parameter ΔV_B as a function of angular momentum ℓ at $E_{\text{c.m.}} = 38.5$ MeV for the $^6\text{Li} + ^{152}\text{Sm} \rightarrow ^{158}\text{Tb}^*$ reaction. It is to be noted that ΔV_B is negative and nonzero for all three choices of fragmentation. It is observed to be least at higher angular momentum and keeps on increasing with a decrease in ℓ value. Hence, we can say that independent of the deformations involved, a large barrier modification is needed for lower angular momentum values. After looking at the behavior of ΔV_B at highest energy, its variation as a

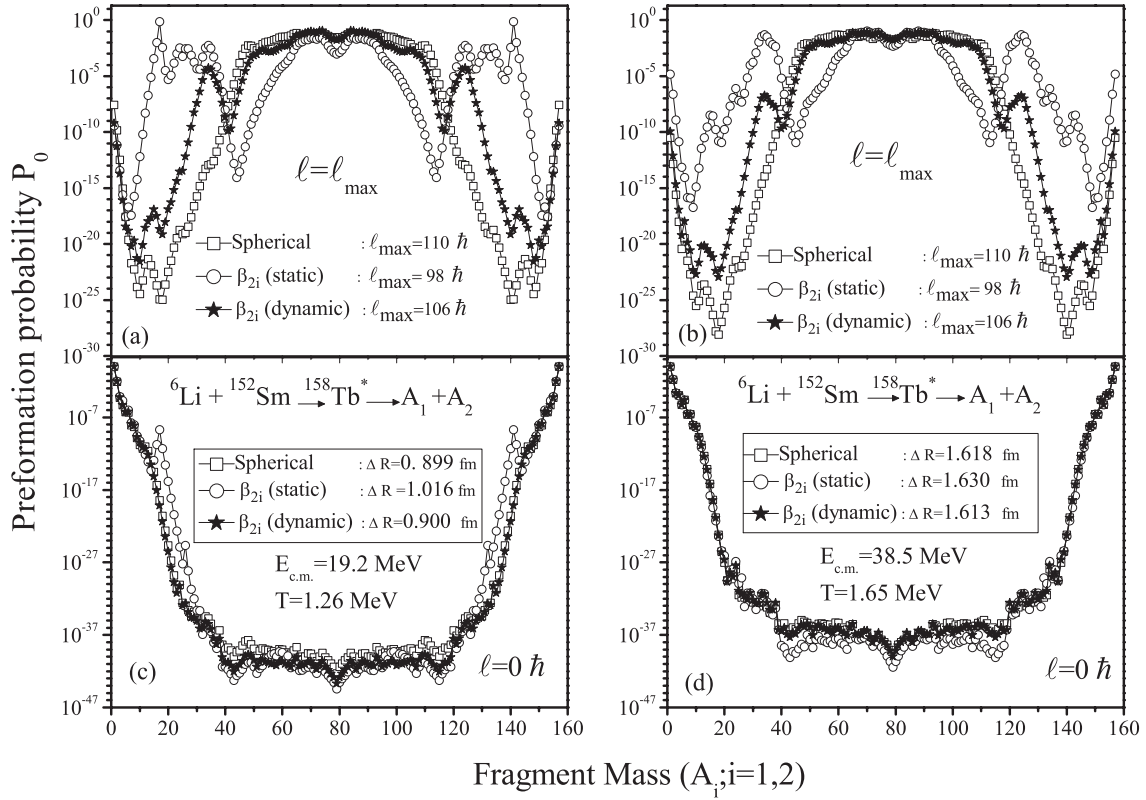


FIG. 3. Preformation probability P_0 as a function of fragment mass, for the decay of compound system $^{158}\text{Tb}^*$, plotted for $\ell = 0 \hbar$ and $\ell = \ell_{\max}$ values, for spherical and deformed nuclei at lowest energy (a), (c) and highest energies (b), (d).

function of $E_{\text{c.m.}}$ for ER channels is shown in Fig. 4(b). This figure shows that at lower energies a large barrier modification is required and it decreases on going from the $1n$ channel to the ^4H channel.

The ER cross sections calculated using DCM for the decay of the $^{158}\text{Tb}^*$ nucleus, with quadrupole static $\beta_{2i}(0)$ deformed choice of fragmentation and compared with the experimental

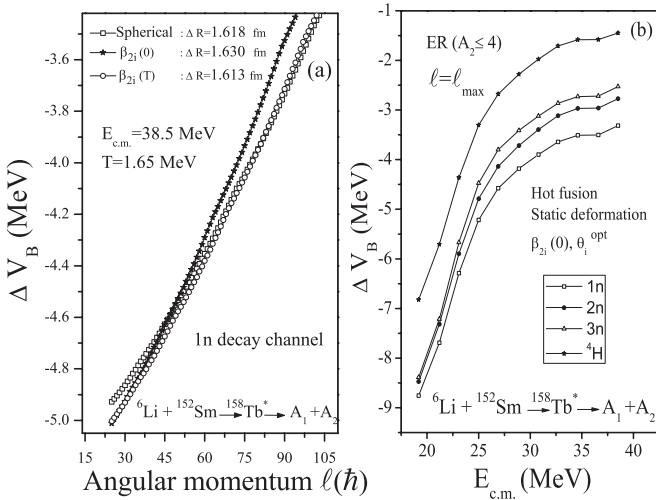


FIG. 4. The barrier lowering parameter ΔV_B (a) as a function of angular momentum at $E_{\text{c.m.}} = 38.5$ MeV. (b) As a function of center-of-mass energy $E_{\text{c.m.}}$ at $\ell = \ell_{\max}$.

data, are tabulated in Table I. Corresponding to the fitted ER cross sections, the ΔR values are depicted in Fig. 5(a). The variation of ΔR as a function of center-of-mass energy ($E_{\text{c.m.}}$) for an incomplete fusion (ICF) process is shown in Fig. 5(b) and will be discussed later in Sec. III C. Calculations are made

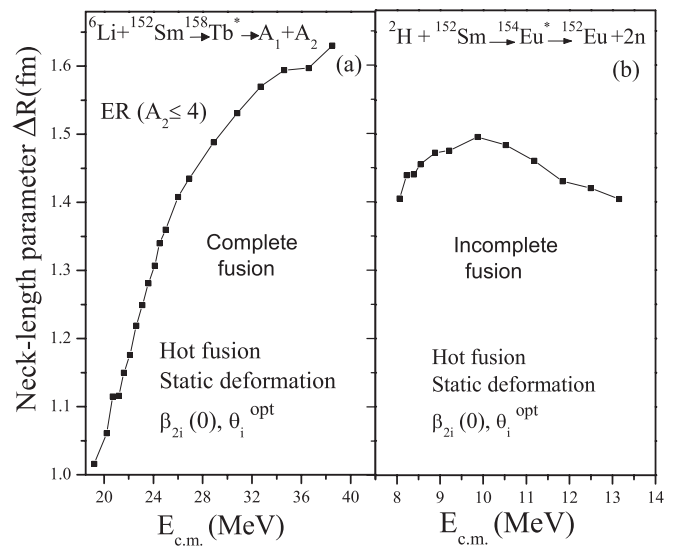


FIG. 5. (a) The best fitted neck-length parameter ΔR , as a function of $E_{\text{c.m.}}$, for the $^{6}\text{Li} + ^{152}\text{Sm}$ reaction as a complete fusion process (CF). (b) Same as (a) but for the ICF process in the $^2\text{H} + ^{152}\text{Sm}$ reaction.

TABLE I. The decay cross sections for evaporation residues ERs calculated using DCM for the $^{158}\text{Tb}^*$ nucleus formed in the ${}^6\text{Li} + {}^{152}\text{Sm}$ reaction with the inclusion of quadrupole static ($\beta_{2i}(0)$) deformation, at all $E_{\text{c.m.}}$ values and at $\ell_{\text{max}} = 98\hbar$, compared with the experimental data of [1].

S. No.	$E_{\text{c.m.}}$ (MeV)	T (MeV)	ΔR_{ER} (fm)	σ^{DCM} (mb)	σ^{Expt} (mb)
1	19.2	1.26	1.016	0.25	0.26 ± 0.05
2	20.2	1.29	1.061	1.03	1.07 ± 0.22
3	20.7	1.30	1.115	1.62	1.77 ± 0.34
4	21.2	1.31	1.116	3.61	3.57 ± 0.45
5	21.6	1.32	1.150	6.52	6.74 ± 0.65
6	22.1	1.33	1.176	9.57	9.64 ± 0.80
7	22.6	1.34	1.219	17.10	17.30 ± 1.5
8	23.1	1.35	1.249	25.80	25.80 ± 2.1
9	23.6	1.36	1.281	38.15	39.70 ± 3.2
10	24.1	1.37	1.307	52.09	53.70 ± 4.3
11	24.5	1.38	1.340	76.50	76.80 ± 6.1
12	25.0	1.39	1.360	96.50	97.00 ± 5.7
13	26.0	1.41	1.408	150.00	151.00 ± 7.0
14	26.9	1.43	1.435	198.00	198.00 ± 9.0
15	28.9	1.47	1.488	304.00	304.00 ± 10
16	30.8	1.51	1.531	417.00	418.00 ± 12
17	32.7	1.54	1.570	560.00	563.00 ± 15
18	34.6	1.58	1.594	634.00	637.00 ± 16
19	36.6	1.61	1.597	705.00	705.00 ± 19
20	38.5	1.65	1.630	792.00	797.00 ± 20

for different neck-length parameters ΔR , chosen to fit the respective experimental data [see Table I and Fig. 5(a)]. It may be noted that neck-length parameter ΔR is a measure

of relative separation between two decaying fragments. Its magnitude is limited within 2 fm, so as to justify the use of the proximity interaction in DCM based calculations. Interestingly, for a majority of compound systems formed in different mass regions [3,4,7], including Fig. 5(a) here, it is observed that ΔR generally increases as a function of incident energy for CF processes. The DCM based calculations reproduce the experimental data for all three approaches, i.e., spherical, static deformed, and dynamical deformed fragmentation paths successfully in terms of single fitting parameter ΔR . We note from Table I that the ER contribution at all energies could reproduce the experimentally measured complete fusion cross sections, thus giving way to the fact that the fission contribution is negligible at all energies, which is in line with the experimental observation. To confirm the same, we have also calculated the fission cross section using DCM at $\Delta R = 0$ fm and 0.5 fm. The reason for taking relatively smaller values of ΔR is that the time scale of the emission of fission fragments is large in comparison to that of ERs [4,6]. In the framework of DCM the neck-length parameter gives a measure of time scale at which the reaction takes place, with a small ΔR indicating a large time scale. With this feature, the fission cross sections were calculated for the most probable fission fragments at $\Delta R = 0$ fm and 0.5 fm and were found to be negligibly small in agreement with the experimental observation.

Experimentally, the ER (complete fusion) cross sections have contributions from the neutron cross sections, $\sum xn$; $x = 2-5$ producing residual nuclei $^{153-156}\text{Tb}$ in the decay of $^{158}\text{Tb}^*$. After having a clear picture about the ER decay channel and the effect of deformations in it, it is of further interest to see the behavior of the potential energy surfaces

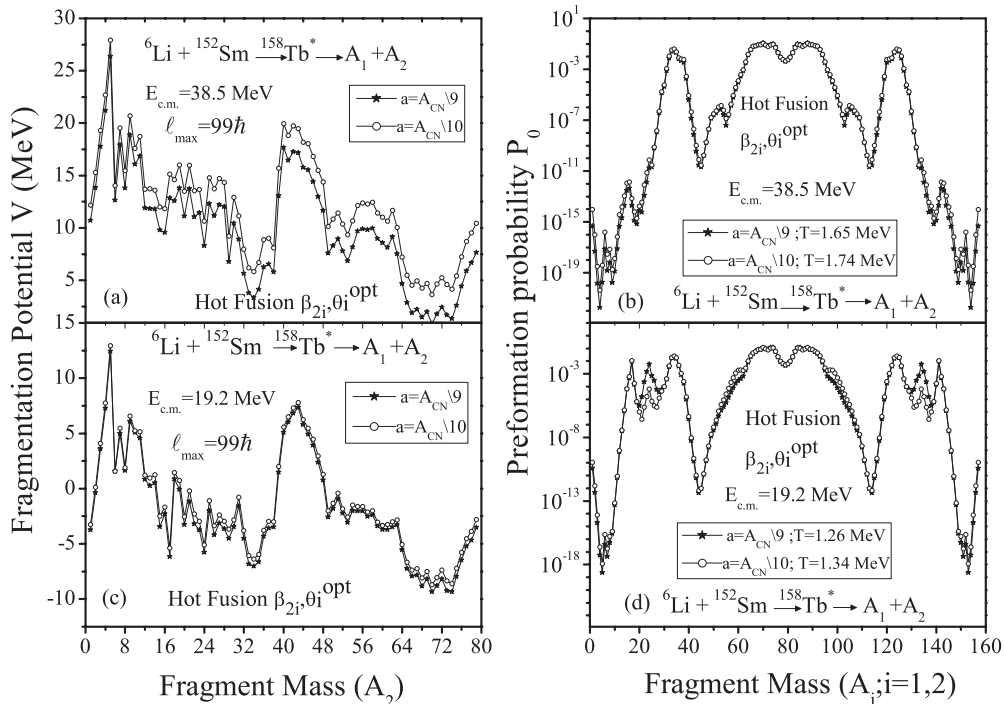


FIG. 6. Effect of level density parameter on (a), (c) fragmentation potential and (b), (d) preformation probability for the neutron decay channel at both extreme energies.

corresponding to neutron cross sections. Initially, using the level density parameter $a = A_{\text{CN}}/9$, the neutron cross sections $\sum xn$; $x = 2-5$ were easily attained at below barrier energy (i.e., $E_{\text{c.m.}} = 19.2$ MeV) but at the highest, above barrier energy (i.e., $E_{\text{c.m.}} = 38.5$ MeV) the same could not be achieved even at maximum allowed value of neck-length parameter ΔR . Henceforth, the calculations were done with higher level density parameter $a = A_{\text{CN}}/10$ through which the cross sections could be attained successfully at two extreme energies across the barrier.

Figure 6 shows the effect of the level density parameter on the fragmentation potential [parts (a), (c)] and preformation probability [parts (b), (d)] for the neutron decay channel at two extreme values of incident energies. The variation is shown only at $\ell = \ell_{\text{max}}$. With an increase in level density 'a' the temperature decreases and the neck-length parameter for the fitted neutron cross sections decreases (from 1.172 fm to 1.164 fm at $E_{\text{c.m.}} = 19.2$ MeV) whereas the ℓ_{max} value remains almost the same. We notice that with the change in level density there is no significant change in the structure of potential energy surfaces (PES), except for an increase in the magnitude of the fragmentation potential observed only at highest energy. Interestingly, in spite of different contributing fragments, the fragmentation behavior for the neutron decay channel is similar to that of the evaporation residue channel [compare Figs. 3(a) and 3(b) with Figs. 6(b) and 6(d)]. It may be noted that neutron decay ($\sum xn$; $x = 2-5$) cross-section data could be addressed at a relatively larger value of neck-length parameter ΔR , in the range of 1.16–2.22 fm, instead of 1.01–1.63 fm for the ER channel. From this observation one may presume that the neck is more elongated for a neutron cluster ($\sum xn$; $x = 2-5$) channel as compared to that for the ER channel.

B. Shell closure and orientation effects in Tb isotopes

To explore the shell closure effect associated with deformations and orientations of decaying fragments we have investigated ${}^6\text{Li} + {}^{144}\text{Sm}$ and ${}^6\text{Li} + {}^{152}\text{Sm}$ reactions at two extreme energies across the Coulomb barrier. The experimental data for the decay of ${}^{150}\text{Tb}^*$ formed in the ${}^6\text{Li} + {}^{144}\text{Sm}$ reaction is taken from [13] and the ER (complete fusion) cross section for the same are fitted using DCM. The calculations have been done for quadrupole static deformation $\beta_{2i}(0)$ within the optimum orientation approach. The isotopic effect observed due to the addition of 8 neutrons to the ${}^{150}\text{Tb}^*$ nucleus can be better analyzed from Fig. 7, where the fragmentation potential $V(A_2)$ is plotted as a function of light fragment mass A_2 . The interesting feature obtained from this figure is that there is no noticeable change in the behavior of fragmentation path in going from the ${}^{150}\text{Tb}^*$ and ${}^{158}\text{Tb}^*$ system at $\ell = 0\hbar$ but it changes significantly at $\ell = \ell_{\text{max}}$. For the lighter system ${}^{150}\text{Tb}^*$ the fission distribution seems more asymmetric as compared to that for the ${}^{158}\text{Tb}^*$ nucleus. A considerable change in PES is observed in going from minimum to maximum energy, which is clarified further in Fig. 8. At both energies, the magnitude of the fragmentation potential of the ${}^{158}\text{Tb}^*$ nucleus is relatively higher for the majority of decaying fragments.

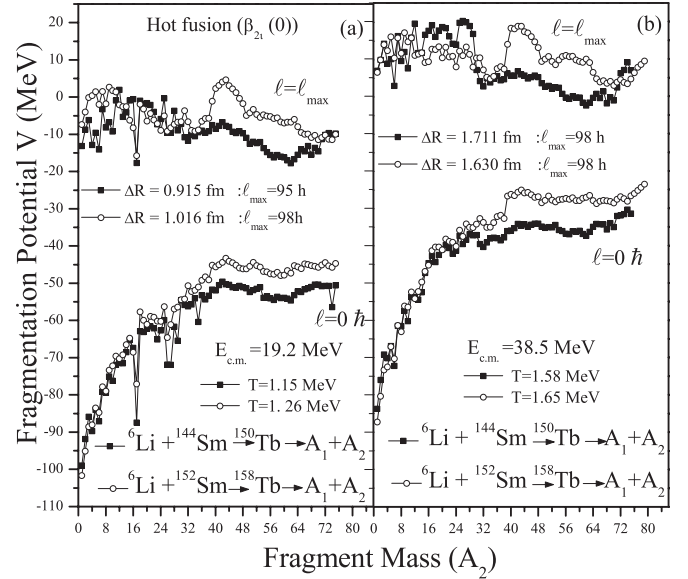


FIG. 7. Fragmentation potential as a function of light fragment mass A_2 for ${}^{150}\text{Tb}^*$ and ${}^{158}\text{Tb}^*$ channels at (a) $E_{\text{c.m.}} = 19.2$ MeV and (b) $E_{\text{c.m.}} = 38.5$ MeV.

Figure 8 shows the variation of preformation probability P_0 as a function of fragment mass A_i for ${}^6\text{Li} + {}^{144}\text{Sm} \rightarrow {}^{150}\text{Tb}^*$ and ${}^6\text{Li} + {}^{152}\text{Sm} \rightarrow {}^{158}\text{Tb}^*$ reactions at $E_{\text{c.m.}} = 19.2$ MeV and $E_{\text{c.m.}} = 38.5$ MeV. It is clear from this figure that the fission pattern remains the same, i.e., asymmetric for both isotopes. However, for the ${}^{150}\text{Tb}^*$ isotope it is relatively more asymmetric than that for ${}^{158}\text{Tb}^*$. Moreover, a heavier isotope favors the heavy mass fragment (HMF) contribution to a greater extent as compared to the lighter one. Thus a

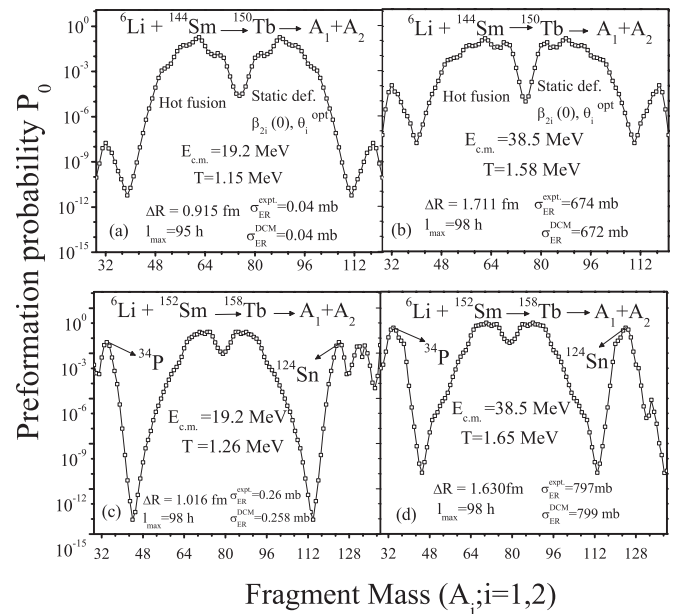


FIG. 8. Preformation probability as a function of fragment mass A_i for the ${}^{150}\text{Tb}^*$ (a), (b) and ${}^{158}\text{Tb}^*$ (c), (d) channels at $E_{\text{c.m.}} = 19.2$ MeV and $E_{\text{c.m.}} = 38.5$ MeV for quadrupole static ($\beta_{2i}(0)$) deformation.

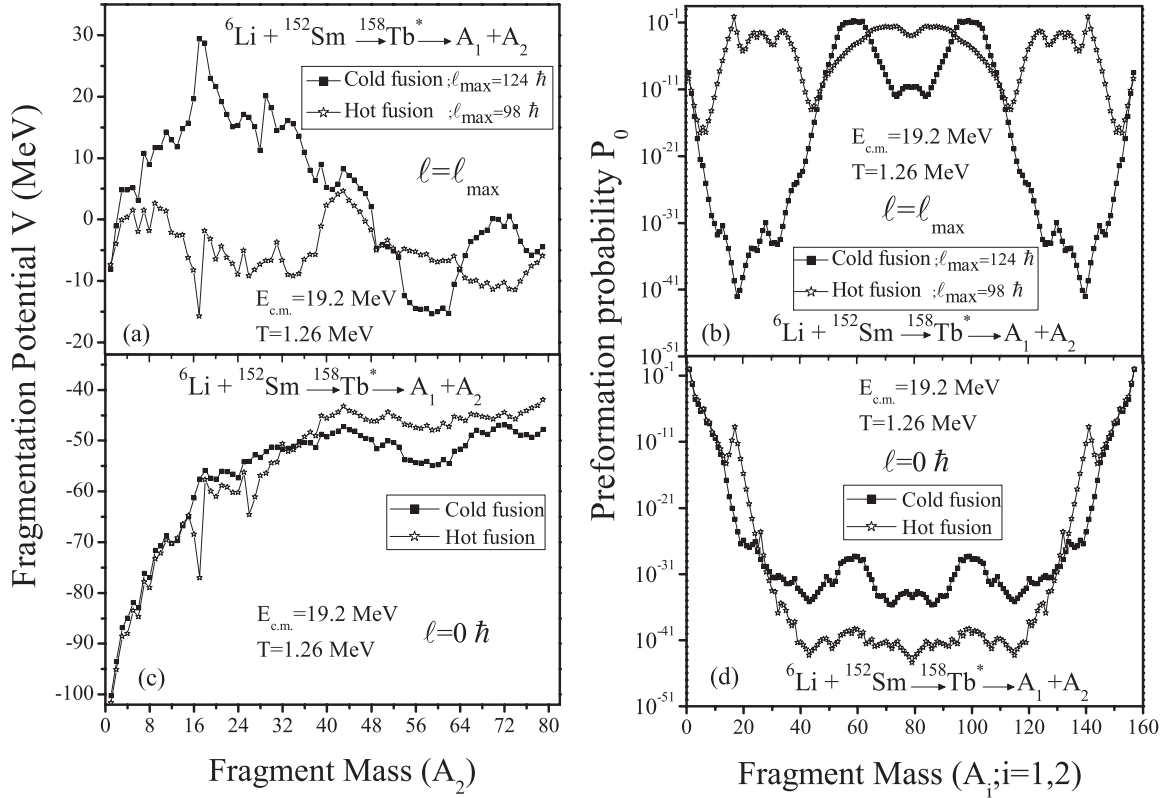


FIG. 9. (a), (c) Fragmentation potential as a function of light fragment mass number (A_2). (b), (d) The variation of preformation probability P_0 as a function of fragment mass (A_i) for decay of the $^{158}\text{Tb}^*$ nucleus formed in the ${}^6\text{Li} + {}^{152}\text{Sm}$ reaction at $E_{\text{c.m.}} = 19.2$ MeV for cold polar and hot equatorial configuration.

significant change in the HMF region is observed with the increase in the isospin N/Z ratio of the decaying Tb compound systems. Interestingly, the shell effects (magic shells) play an important role in the fragment mass distribution for the ${}^6\text{Li} + {}^{152}\text{Sm}$ reaction at both extreme energies giving rise to a high preformation probability for the ${}^{34}\text{P}$ ($Z = 15$, $N = 19$) fragment and its complement ${}^{124}\text{Sn}$ ($Z = 50$, $N = 74$) [see Figs. 8(c) and 8(d)]. It must be noted that this shoulder signifies the importance of shell effects as ${}^{34}\text{P}$ seems to be originated due to nearby neutron shell closure $N = 20$. Similarly, ${}^{124}\text{Sn}$ corresponds to magic proton shell closure $Z = 50$. On the other hand, no such highly preformed peak is observed for the lighter mass ${}^{150}\text{Tb}^*$ nucleus [see Figs. 8(a) and 8(b)]. This difference in preformation probability shows that shell closure effects of decaying fragments are more prominent for deformed targets like ${}^{152}\text{Sm}$, and are nearly absent in spherical target ${}^{144}\text{Sm}$. It is relevant to mention here that in earlier work [4,12] similar effects were seen in the decay of ${}^{202}\text{Pb}$ formed via the ${}^{152}\text{Sm}$ target and the appearance of such an asymmetric peak was associated with the possibility of quasifission. Although quasifission may not be appearing in the chosen asymmetric reaction, but this asymmetric peak at $A_2 = 34$ (and complementary fragment $A_1 = 124$) seems to suggest that some other competing decay mechanism is in operation for the ${}^6\text{Li} + {}^{152}\text{Sm} \rightarrow {}^{158}\text{Tb}^*$ reaction.

Evidently, apart from the role of deformations, the orientation degree of freedom holds equal importance as far as heavy ion reaction dynamics is concerned. Thus, after

having an insight of static and dynamic deformations and the shell closure effects, we intend to investigate explicitly the role of orientation degrees of freedom in the decay of the ${}^{158}\text{Tb}^*$ nucleus formed in the ${}^6\text{Li} + {}^{152}\text{Sm}$ reaction. In general, for actinide targets being prolate deformed there lies a possibility that the projectile may hit the ‘equatorial’ region of the deformed target and hence possess the most ‘compact’ configuration on its way to compound nucleus formation. Interestingly, this orientation may depend on the energy of the colliding nuclei, so with the change in energy from above barrier to below barrier, a change in orientation may also be observed. At below barrier energy, the probability of the projectile to hit the deformed target in ‘polar’ region is feasible, giving rise to ‘elongated’ configuration [10,27]. Since for the ${}^6\text{Li} + {}^{152}\text{Sm} \rightarrow {}^{158}\text{Tb}^*$ reaction, ${}^{152}\text{Sm}$ is a prolate deformed target, so it would be of interest to see the effect of orientation at below barrier energy for this lanthanide system. In order to pursue this, a comparative analysis of equatorial and polar configurations in the decay of the ${}^{158}\text{Tb}^*$ nucleus has been done. We have carried out the comparison of hot equatorial (compact) and cold polar (noncompact) orientations by considering quadrupole static $\beta_{2i}(0)$ deformation and the optimum orientation approach. The equatorial compact orientations have the smallest interaction radius and highest barrier height, while the polar elongated orientations have the largest interaction radius and lowest barrier height [10]. Figures 9(a) and 9(c) show the variation of the fragmentation potential as a function of light fragment mass (A_2) at

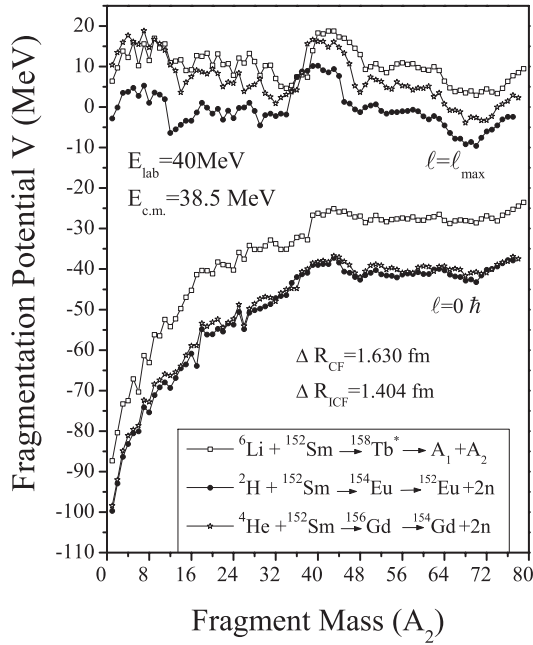


FIG. 10. Fragmentation potential $V(\eta)$ for fragments formed in the ${}^6\text{Li} + {}^{152}\text{Sm}$ reaction (CF) as well as by a reaction induced by ${}^2\text{H}$ and ${}^4\text{He}$ (ICF) (due to the break-up of ${}^6\text{Li}$) at $E_{\text{c.m.}} = 38.5$ MeV for quadrupole static ($\beta_{2i}(0)$) deformation.

$E_{\text{c.m.}} = 19.2$ MeV for both hot equatorial and cold polar orientations. From the figure it is clear that the effect of orientation is more pronounced at higher angular momentum, $\ell = \ell_{\text{max}}$ as compared to $\ell = 0\hbar$. Interestingly, hot equatorial orientations favor symmetric fragment mass distribution, whereas for the cold polar orientations, an asymmetric fragmentation is preferred. This mass distribution is also supported by Figs. 9(b) and 9(d) which shows preformation probability as a function of fragment mass (A_i). One may clearly see from this figure that the orientations are sensitive to the angular momentum effect. At minimum ℓ value, i.e., $\ell = 0\hbar$ no such change in preformation probability and hence the fragment distribution is noticed [see Figs. 9(c) and 9(d)]. On the contrary, a strong variation in mass distribution from symmetric to asymmetric fragmentation is observed in going from equatorial to polar orientations at maximum angular momentum, $\ell = \ell_{\text{max}}$ [see Figs. 9(a) and 9(b)]. The symmetric mass distribution observed at ℓ_{max} for equatorial orientation favors the IMFs and HMFs in its decay, which are highly suppressed for the polar choice of orientation. The neck-length parameter ΔR and the ℓ_{max} value are different for both cases being higher for polar orientation (1.070 fm and $124\hbar$) as compared to that for equatorial orientation (1.016 fm and $98\hbar$). From the above discussion it may be concluded that the orientation of decaying fragments and the associated shell closure effects play an important role in the decay of intermediate mass nucleus ${}^{158}\text{Tb}^*$.

C. Incomplete fusion due to the break-up of ${}^6\text{Li}$

The concept of the partial fusion of a projectile in heavy-ion interactions was set first with the experimental observation by Britt and Quinton [28]. This process of partial fusion due

to the breakup of the original projectile was coined as the incomplete fusion process (ICF). In a qualitative way both complete fusion (CF) and incomplete fusion (ICF) processes can be disentangled on the basis of the type of interaction or angular momentum. In a complete fusion process, the compound nucleus formed after intimate contact involves an amalgamation of the entire projectile with the target mass. Thus, the whole of the angular momentum and the kinetic energy is distributed amongst all degrees of freedom of the compound nucleus. However with noncentral interactions [29–31], higher angular momentum values are imparted and, as a consequence of this entire fusion of the projectile, is hindered giving way to ICF. Wilczynski *et al.* [32] has established ICF to be an extension of CF for higher angular momentum values associated with the noncentral interactions. Extensive work has also been carried out on CN and nCN processes by Morgenstern *et al.* [33] that provides a correlation between the fraction of ICF and center-of-mass velocity with mass asymmetry in the entrance channel. The systematics presented by Morgenstern *et al.* have shown that the ICF component contributes more towards the total reaction cross sections for mass asymmetric systems as compared to mass symmetric systems. All these studies have helped in understanding the dynamics of ICF, its dependence on beam energy and entrance channel mass asymmetry.

The experiment carried out to study the decay cross sections formed in the ${}^6\text{Li} + {}^{152}\text{Sm} \rightarrow {}^{158}\text{Tb}^*$ reaction [1] shows that CF cross sections are suppressed by $\sim 28\%$. This suppression is associated with the break-up of loosely bound projectile ${}^6\text{Li}$ into two fragments, ${}^2\text{H}$ and ${}^4\text{He}$. Based on these results, the ICF cross sections for the break-up of ${}^6\text{Li}$ have been studied by considering the ${}^2\text{H}$ channel. In the framework of DCM the calculations for ICF have been done by applying relevant and necessary energy corrections [9] to obtain the energy of the new projectile involved. The calculations have been done by

TABLE II. The ICF decay cross sections for the $2n$ emission channel calculated using DCM with static quadrupole ($\beta_{2i}(0)$) deformation for the ${}^{154}\text{Eu}^*$ nucleus formed in the ${}^2\text{H} + {}^{152}\text{Sm}$ reaction at all corrected $E_{\text{c.m.}}$ values lying above the Coulomb barrier compared with experimental incomplete fusion (ICF) data [1]. Also the ΔR values corresponding to the fitted cross sections for the ${}^2\text{H}$ channel are tabulated.

S. No.	$E_{\text{c.m.}}$ (MeV)	T (MeV)	ΔR_{2n} (fm)	$\sigma_{\text{ICF}}^{\text{DCM}}$ (mb)	$\sigma_{\text{ICF}}^{\text{EXPT.}}$ (mb)
1	8.060	1.051	1.405	14.94	14.980
2	8.225	1.056	1.439	18.74	19.250
3	8.389	1.061	1.440	20.50	20.760
4	8.547	1.065	1.455	23.20	23.230
5	8.883	1.075	1.472	28.41	28.510
6	9.208	1.084	1.475	28.90	29.018
7	9.870	1.102	1.495	30.60	31.350
8	10.521	1.119	1.483	29.20	29.375
9	11.182	1.137	1.460	24.00	24.803
10	11.844	1.154	1.430	18.00	18.121
11	12.495	1.171	1.420	16.13	16.298
12	13.156	1.188	1.404	13.72	13.762

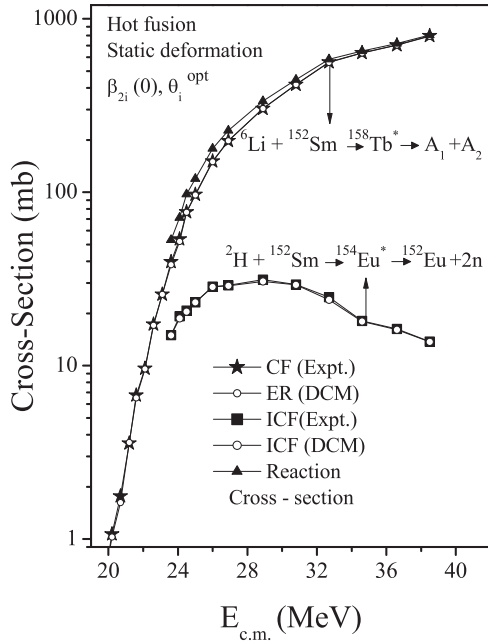


FIG. 11. Comparison of DCM cross sections having contribution from complete fusion and incomplete fusion processes with experimental data at different center-of-mass energies.

taking the quadrupole static ($\beta_{2i}(0)$) deformation into account. Experimentally the dominant decay mode for d -capture is the $2n$ emission process and cross sections for the same have been calculated. The fitted cross sections at various corrected energies for the ${}^2\text{H}$ channel with the corresponding ΔR values are tabulated in Table II. The variation of the fragmentation potential, $V(\text{MeV})$ as a function of light fragment mass (A_2) is shown for ${}^6\text{Li}$ (CF), ${}^2\text{H}$ (ICF), and ${}^4\text{He}$ (ICF) channels in Fig. 10. The ${}^4\text{He}$ (ICF) channel fragmentation path is shown at the same ΔR value as that for the ${}^2\text{H}$ case. From Fig. 10, one may observe that the overall fragmentation path is almost similar in CF and ICF process at two extreme values of angular momentum. Another point of interest here is that contrary to the CF process, ΔR for ICF does not increase as a function of $E_{\text{c.m.}}$ [compare Fig. 5(a) with Fig. 5(b)]. In the latter case it remains almost constant around $\Delta R = 1.45$ fm with a structure similar to that of the ICF cross section. The DCM based ICF cross sections are found to have a good agreement with the experimental data [1].

Finally, a comparative study of calculated DCM cross sections with experimental data showing contributions of CF (ER) and ICF processes is shown in Fig. 11. It may be noted that the evaporation residue channel is the major contributor towards complete fusion cross sections with fission contribution being negligibly small at a reported energy range. Also the behavior of incomplete fusion is depicted in this figure, which shows that ICF contributes significantly towards the total reaction cross section. Figure 11 clearly shows that the

DCM based ER and ICF cross sections are in nice agreement with the experimental data.

IV. SUMMARY

We observe that both deformations and orientations have a significant effect on the decay process of the lanthanide system ${}^{158}\text{Tb}^*$. The role of static and dynamic deformations is studied within the framework of DCM for the ${}^6\text{Li} + {}^{152}\text{Sm} \rightarrow {}^{158}\text{Tb}^*$ reaction over a wide range of incident energies spread on either side of the Coulomb barrier. We are able to account reasonably well for complete fusion cross sections having a major contribution from the ER channel at various incident energies within a single parameter description ΔR , for spherical as well as for static and dynamic choices of deformation up to quadrupole (β_{2i}). The fragment mass distribution varies with the inclusion of deformations. This may be due to the preformation factor P_0 which gets modified with the inclusion of deformations and hence changes the fragment mass distribution. The deformations play a silent role at $\ell = 0\hbar$, whereas they become indispensable at $\ell = \ell_{\text{max}}$. The neck-length parameter ΔR is almost similar for spherical and dynamic $\beta_{2i}(T)$ deformed choices of fragmentation whereas, it is higher in magnitude for static deformed consideration. In addition to this, the effect of hot equatorial (compact) and cold polar (noncompact) orientation is explored in the decay of the ${}^{158}\text{Tb}^*$ nucleus. For equatorial orientation, IMF and HMF components seem more prominent which are otherwise suppressed for polar orientation. Moreover, the fragment mass distribution changes from symmetric to asymmetric distribution while going from equatorial to polar orientations. With the change in level density parameter no significant change in potential energy surfaces (PES) is observed for the $\sum xn; x = 2-5$ cross sections. Interestingly the fragmentation structure of the $\sum xn; x = 2-5$ decay channel is similar to that of ER, despite the fact that the contributing fragments are not the same in both of them. The N/Z dependence of decay fragments in Tb isotopes is explored and it is observed that the neutron-rich ${}^{158}\text{Tb}^*$ nucleus formed with the deformed target ${}^{152}\text{Sm}$ gives enhanced cross sections for ${}^{34}\text{P}$ ($Z = 15, N = 19$) and its complementary fragment ${}^{124}\text{Sn}$ ($Z = 50, N = 74$) which otherwise are suppressed for ${}^{150}\text{Tb}^*$ nuclei formed with spherical target ${}^{150}\text{Sm}$. This observation enables us to conclude that the shell closure effect of the decaying fragment are more prominent for reactions with a deformed target as compared to spherical targets. In addition to this, the contribution of the noncompound nucleus through ICF process is also worked out and it is observed that the structure of fragmentation paths is similar for both CF and ICF processes.

ACKNOWLEDGMENTS

The financial support from the Department of Science and Technology (DST), New Delhi is gratefully acknowledged.

[1] P. K. Rath, S. Santra, N. L. Singh, K. Mahata, R. Palit, B. K. Nayak, K. Ramachandran, V. V. Parkar, R. Tripathi,

S. K. Pandit, S. Appannababu, N. N. Deshmukh, R. K. Choudhry, and S. Kailas, *Nucl. Phys. A* **874**, 14 (2012).

- [2] R. K. Gupta, M. Balasubramaniam, R. Kumar, D. Singh, and C. Beck, *Nucl. Phys. A* **738**, 479c (2004); R. K. Gupta, M. Balasubramaniam, R. Kumar, D. Singh, C. Beck, and W. Greiner, *Phys. Rev. C* **71**, 014601 (2005).
- [3] B. B. Singh, M. K. Sharma, R. K. Gupta, and W. Greiner, *Int. J. Mod. Phys. E* **15**, 699 (2006); B. B. Singh, M. K. Sharma, and R. K. Gupta, *Phys. Rev. C* **77**, 054613 (2008).
- [4] S. Kanwar, M. K. Sharma, B. B. Singh, R. K. Gupta, and W. Greiner, *Int. J. Mod. Phys E* **18**, 1453 (2009).
- [5] R. K. Gupta, in *Clusters in Nuclei*, Lecture Notes in Physics 818 edited by C. Beck (Springer-Verlag, Berlin/Heidelberg, 2010), Vol. I, p. 223; S. K. Arun, R. Kumar, and R. K. Gupta, *J. Phys. G: Nucl. Part. Phys.* **36**, 085105 (2009).
- [6] M. K. Sharma, S. Kanwar, G. Sawhney, R. K. Gupta, and W. Greiner, *J. Phys. G: Nucl. Part. Phys.* **38**, 055104 (2011); D. Jain, R. Kumar, M. K. Sharma, and R. K. Gupta, *Phys. Rev. C* **85**, 024615 (2012).
- [7] M. K. Sharma, G. Sawhney, R. K. Gupta, and W. Greiner, *J. Phys. G: Nucl. Part. Phys.* **38**, 105101 (2011); G. Sawhney, R. Kumar, and M. K. Sharma, *Phys. Rev. C* **86**, 034613 (2012).
- [8] G. Sawhney, M. K. Sharma, and R. K. Gupta, *Phys. Rev. C* **83**, 064610 (2011); K. Sandhu, M. K. Sharma, and R. K. Gupta, *ibid.* **85**, 024604 (2012).
- [9] G. Kaur and M. K. Sharma, *Nucl. Phys. A* **884**, 36 (2012); M. Kaur, R. Kumar, and M. K. Sharma, *Phys. Rev. C* **85**, 014609 (2012).
- [10] R. K. Gupta, M. Balasubramaniam, R. Kumar, N. Singh, M. Manhas, and W. Greiner, *J. Phys. G: Nucl. Part. Phys.* **31**, 631 (2005); R. K. Gupta, M. Manhas, and W. Greiner, *Phys. Rev. C* **73**, 054307 (2006).
- [11] M. G. Itkis *et al.*, *Nucl. Phys. A* **734**, 136 (2004).
- [12] A. M. Stefanini *et al.*, *Eur. Phys. J. A* **23**, 473 (2005).
- [13] P. K. Rath, S. Santra, N. L. Singh, R. Tripathi, V. V. Parkar, B. K. Nayak, K. Mahata, R. Palit, S. Kumar, S. Mukherjee, S. Appannababu, and R. K. Choudhry, *Phys. Rev. C* **79**, 051601(R) (2009).
- [14] L. F. Canto, P. R. S. Gomes, R. Donangelo, and M. S. Hussein, *Phys. Rep.* **424**, 1 (2006), and references therein.
- [15] M. Dasgupta, P. R. S. Gomes, D. J. Hinde, S. B. Moraes, R. M. Anjos, A. C. Berriman, R. D. Butt, N. Carlin, J. Lubian, C. R. Morton, J. O. Newton, and A. Szanto de Toledo, *Phys. Rev. C* **70**, 024606 (2004).
- [16] R. K. Gupta and W. Greiner, in *Heavy Elements and Related New Phenomenon*, edited by W. Greiner and R. K. Gupta (World Scientific, Singapore, 1999), Vol. I, Chap. 14, p. 536.
- [17] J. Maruhn and W. Greiner, *Z. Phys.* **251**, 431 (1972); R. K. Gupta, W. Scheid, and W. Greiner, *Phys. Rev. Lett.* **35**, 353 (1975).
- [18] R. K. Gupta, M. K. Sharma, S. Singh, R. Nouicer, and C. Beck, *Phys. Rev. C* **56**, 3242 (1997); R. K. Gupta, M. K. Sharma, N. V. Antonenko, and W. Scheid, *J. Phys. G: Nucl. Part. Phys.* **25**, L47 (1999); M. K. Sharma, R. K. Gupta, and W. Scheid, *ibid.* **26**, L45 (2000).
- [19] N. J. Davidson, S. S. Hsiao, J. Markram, H. G. Miller, and Y. Tzeng, *Nucl. Phys. A* **570**, 61c (1994).
- [20] R. K. Gupta, R. Kumar, N. K. Dhiman, M. Balasubramaniam, W. Scheid, and C. Beck, *Phys. Rev. C* **68**, 014610 (2003).
- [21] G. Audi, A. H. Wapstra, and C. Thibault, *Nucl. Phys. A* **729**, 337 (2003); G. Audi and A. H. Wapstra, *ibid.* **595**, 409 (1995).
- [22] W. Myers and W. J. Swiatecki, *Nucl. Phys.* **81**, 1 (1966).
- [23] G. Royer and J. Mignen, *J. Phys. G: Nucl. Part. Phys.* **18**, 1781 (1992).
- [24] P. Möller, J. R. Nix, W. D. Myers, and W. J. Swiatecki, *At. Nucl. Data Tables* **59**, 185 (1995).
- [25] M. Muenchow and W. Scheid, *Phys. Lett. B* **162**, 265 (1985); *Nucl. Phys. A* **468**, 59 (1987).
- [26] M. Rashdan, A. Faessler, and W. Wadia, *J. Phys. G: Nucl. Part. Phys.* **17**, 1401 (1991).
- [27] K. Nishio, H. Ikezoe, S. Mitsuoka, I. Nishinaka, Y. Nagame, Y. Watanabe, T. Ohtsuki, K. Hirose, and S. Hofmann, *Phys. Rev. C* **77**, 064607 (2008); K. Sandhu, M. K. Sharma, and R. K. Gupta, *ibid.* **86**, 064611 (2012).
- [28] H. C. Britt and A. R. Quinton, *Phys. Rev.* **124**, 877 (1961).
- [29] K. A. Geoffroy, D. G. Sarantites, M. L. Halbert, D. C. Hensley, R. A. Dayras, and J. H. Barker, *Phys. Rev. Lett.* **43**, 1303 (1979).
- [30] W. Trautmann, O. Hansen, H. Tricoire, W. Hering, R. Ritzka, and W. Trombik, *Phys. Rev. Lett.* **53**, 1630 (1984).
- [31] T. Inamura *et al.*, *Phys. Lett. B* **68**, 51 (1977); **84**, 71 (1982); T. Inamura, A. C. Kahler, D. R. Zolnowski, U. Garg, T. T. Sugihara, and M. Wakai, *Phys. Rev. C* **32**, 1539 (1985).
- [32] J. Wilczynski *et al.*, *Phys. Rev. Lett.* **45**, 606 (1980); *Nucl. Phys. A* **373**, 109 (1982).
- [33] H. Morgenstern, W. Bohne, W. Galster, K. Grabisch, and A. Kyanowski, *Phys. Rev. Lett.* **52**, 1104 (1984); H. Morgenstern *et al.*, *Z. Phys. A* **313**, 39 (1983).